Materials Today Sustainability 24 (2023) 100509

Contents lists available at ScienceDirect

Materials Today Sustainability

journal homepage: https://www.journals.elsevier.com/materials-today-sustainability

Activated three-dimensionally ordered micromesoporous carbons for CO_2 capture

M. Vorokhta [a, *], J. Nováková [b], M. Dopita [c], I. Khalakhan [b], V. Kopecký [d], M. Švábová [a]

[a] Department of Geochemistry, Institute of Rock Structure and Mechanics, Czech Academy of Sciences, V Holešovičkách 94/41, 18209, Prague 8, Czech Republic
[b] Department of Surface and Plasma Science, Faculty of Mathematics and Physics, Charles University, V Holešovičkách 2, 18000, Prague 8, Czech Republic
[c] Department of Condensed Matter Physics, Faculty of Mathematics and Physics, Charles University, Ke Karlovu 5, 121 16, Prague 2, Czech Republic
[d] Division of Biomolecular Physics, Institute of Physics, Faculty of Mathematics and Physics, Charles University, Ke Karlovu 5, 121 16, Prague 2, Czech Republic

ARTICLE INFO

Article history:
Received 13 April 2023
Received in revised form
31 July 2023
Accepted 17 August 2023
Available online 20 August 2023

Keywords:
3DOmm carbon
Physical activation
CO_2 adsorption
Selectivity
Isosteric heat

ABSTRACT

Three-dimensionally ordered micromesoporous carbon (3DOmm) has been studied recently as a potential sorbent for CO_2 capture at higher pressures. However, the as-synthesized material usually has a low microporous fraction, which could significantly limit CO_2 uptake. Herein, we showed that microporosity in 3DOmm carbon can be increased by physical activation, substantially improving its CO_2 capture performance in the wide pressure range. The highly porous activated 3DOmm carbons, having amorphous structure, were prepared with ordered spherical mesopores of diameter 22.7–24.7 nm and ultramicropores in the walls of diameter 0.41–0.55 nm. Physical activation was performed by exposing the post-synthesized 3DOmm carbon to high temperatures of 973–1173 K under a CO_2 flow for 30 min. The activation procedure did not show any visible destruction of the ordered mesoporous structure in the 3DOmm carbon. However, it had a significant impact on micropore and mesopore volumes and the specific surface area, which in turn affected the CO_2 adsorption capacity of the carbons. Accordingly, after activation at 973 K, the micropore volume of 0.23 cm^3/g, the mesopore volume of 3.70 cm^3/g and the specific surface area of 1058 m^2/g in the 3DOmm carbon increased to 0.27 cm^3/g, 3.94 cm^3/g and 1462 m^2/g, respectively. Further increase in activation temperature led to decreasing pore values due to widening and shrinking of the thin carbon walls in the 3DOmm carbon. The 3DOmm carbon activated at 973 K had the highest micropore and mesopore volumes and the highest CO_2 adsorption performance over the whole pressure range (3.19 mmol/g at 273 K and 100 kPa; 11.18 mmol/g at 298 K and 2 MPa and 0.38 mmol/g under flue 15% CO_2/85% N_2 gas conditions at 298 K). All 3DOmm carbons showed fast kinetics, high selectivity for CO_2 over N_2 (33.2–51.5), the excellent regenerative ability and isosteric heats (18.9–29.2 kJ/mol), indicating physical adsorption.

1. Introduction

Climate change that has been taking place over recent decades has become a major concern for human society [1]. Carbon dioxide is considered the main greenhouse gas, playing a central role in raising the global atmospheric temperature [2]. Since 1950, atmospheric CO_2 levels have risen from 280 ppm (parts per million) to 419 ppm as a result of industrial activity, which is more than any increase that took place over the pre-industrial 20,000 years (from 185 ppm at the Last Glacial Maximum to 280 ppm in 1850). Such a rapid increase in CO_2 levels in the atmosphere has resulted in the average Earth temperature increasing by ~2° Celsius during the 20th century [3]. If CO_2 emissions are not reduced, atmospheric CO_2 levels are predicted to increase to 550 ppm by 2100 [4].

Considerable efforts have been made to develop strategies for increasing the effectiveness of CO_2 reduction in the atmosphere. Some approaches include CO_2 capture from stationary sources, where the concentration of CO_2 is very high, or the capturing of CO_2 gas directly from the atmosphere, where the concentration of CO_2 gas is low [5]. Because the main stationary sources are considered to be the flue gases of coal-fired power plants, emitting about 40% of the average CO_2 levels in the atmosphere [5,6], methods for

* Corresponding author.
E-mail address: vorokhta@irsm.cas.cz (M. Vorokhta).

https://doi.org/10.1016/j.mtsust.2023.100509
2589-2347/

capturing CO_2 from power plant sources are critical. There are a few methods, including pre-combustion capture, post-combustion capture, oxy-fuel combustion and chemical looping combustion [7,8]. Adsorption onto solid adsorbents is one of the methods used in the case of post-combustion capture at low pressures [4] and pre-combustion capture at elevated pressures [9]. Pre-combustion capture implies the gasification of fuel and air/O_2, resulting in CO and H_2 syngas. The CO then reacts with steam to yield CO_2 and H_2, followed by their separation. Post-combustion capture technology is based on CO_2 capture from the flue gas after combustion. Typically, flue gas contains a low concentration of CO_2 (~15 vol %) [10].

The capture of CO_2 using adsorbents is attracting increased attention due to its simplicity, low cost, high capture efficiency and low energy consumption [11–13]. Many academic studies have therefore aimed at developing inexpensive and efficient adsorbents for CO_2 capture [14–17]. Among different adsorbents, porous carbon materials have shown promising results in CO_2 capture over a wide range of pressures and temperatures [18–20]. High efficiency CO_2 capture by carbon materials at atmospheric pressure was observed in the presence of a large volume of micropores, especially ultramicropores less than ~0.7 nm [21–23]. In contrast, mesopores played a significant role at higher pressures [24,25].

Surface modification of carbon materials with different functional groups also significantly affects CO_2 adsorption capacity [26,27]. In particular, oxygen-containing groups showed an attractive force to CO_2, for example, in activated coal chars [28] and pyrazole-derived micromesoporous carbons [29]. The nitrogen content in the carbon structure enhances CO_2 adsorption in the case of microporous carbons [22] and hydrochar-derived microporous carbons [30], carbon-based monolithic [31], nanoporous carbons prepared from metal-organic framework [32], ordered mesoporous carbons [33], activated carbons [34] and activated carbon fibers [35], and others [36,37]. However, at low pressures, CO_2 adsorption capacity was found to depend on narrow micropores rather than on the total nitrogen content [22,38,39] and specific surface area [11,22,39]. The high micropore content and introduction of nitrogen groups into the carbon structure was found to enhance the selectivity of CO_2 over N_2 as well [40,41]. For example, highly porous nitrogen-doped carbon cryogels, in addition to excellent CO_2 uptake, exhibited the significantly higher CO_2/N_2 selectivity compared to many carbon cryogels that have been reported [42]. Despite the high adsorption capacity of carbon materials modified with nitrogen, the nitrogen groups in the carbon structure can cause an undesirable reduction in regenerative ability of the carbon adsorbent. This is due to the formation of chemical bonds between CO_2 molecules and the carbon surface [43], the breaking of which requires much more energy than for carbon materials with weak Van der Waals forces. Additionally, an excessive amount of nitrogen groups can lead to a decrease in narrow micropores, resulting in a trade-off in CO_2 uptake [44]. Recent studies have reported the preparation of (nitrogen and sulfur)-dual doped porous carbons from sources, such as corn-starch [45] and shrimp shells [46], which exhibit remarkable CO_2 adsorption and CO_2/N_2 selectivity due to Lewis acid-base interactions between CO_2 and heteroatoms at low pressures. Thus, while the presence of heteroatoms has been shown to increase CO_2 uptake at low pressures, micropores less than 1 nm in size play a dominant role in CO_2 adsorption as the pressure approaches atmospheric.

In addition to these factors, the order of the porous structure also influences CO_2 capture. A well-ordered porous carbon structure has a significant advantage over carbon materials with a non-regular pore order because well-developed pores allow CO_2 to reach adsorption sites very quickly, improving the kinetics of the adsorption process [47,48]. Micromesoporous carbons with ordered mesopores have, therefore, attracted a lot of attention due to their significant mesopore volume, specific surface area, perfect regenerative ability, sorption rate, etc. [49,50].

We have recently shown that three-dimensionally ordered micromesoporous carbon (3DOmm) has a potential for CO_2 capture in pre-combustion capture due to its ability to adsorb a tremendous amount of CO_2 at high pressures in a large mesopore volume [51]. But, this carbon did not show such excellent CO_2 capture at atmospheric pressure due to its low microporous volume. Increasing the number of micropores in such types of 3DOmm carbon may lead to improvements in its capture properties at low pressures, also contributing to the higher CO_2 adsorption amount at high pressures. The goal of this work was therefore to prepare a complex 3DOmm adsorbent, providing high CO_2 uptake for a wide pressure range.

Herein, the synthetic process of 3DOmm carbon was improved by submitting as-synthesized 3DOmm carbon to a further stage – physical activation with CO_2 at high temperatures – in order to achieve better micropore characteristics. A novel type of activated carbon materials with ordered mesopores revealed well-developed microporosity, showing that the known 3DOmm structure can be further optimised towards enhanced CO_2 capture. The prepared activated 3DOmm carbons revealed that the activation procedure did not have a destructive impact on the ordered structure, but it impacted significantly on pore volumes, which in turn had an impact on the CO_2 capture performance at different pressures. The CO_2 adsorption capacities of non-activated and activated 3DOmm carbons were determined at atmospheric pressure and pressures up to 2 MPa, and at different temperatures. The relationship between CO_2 molecules and the carbon surface was studied by estimating isosteric heats, depending on the adsorbed amount, and regenerative ability. Separation of CO_2 from N_2 was also evaluated for all 3DOmm carbons studied.

2. Experimental

2.1. Chemicals and gases used

For preparing the SiO_2 nanoparticles, we used L-lysine ($H_2N(CH_2)_4CH(NH_2)CO_2H$, purity of ≥98%), tetraethyl orthosilicate ($Si(OC_2H_5)_4$, purity of 98%) and deionized water. For the carbon synthesis, furfurylalcohol ($C_5H_6O_2$, purity of 98%) as a carbon precursor, oxalic acid ($C_2H_2O_4$, purity of 99%) as an acid catalyst and a solution of 40% hydrofluoric acid as a silica nanoparticle remover were used. All reagents were purchased from Sigma-Aldrich Ltd., Czech Republic.

For the sorption measurements, we used CO_2 gas with purity of 99.995 vol % and N_2 gas with purity of 99.995 vol % from Linde Gas Ltd., Czech Republic.

2.2. Preparation and activation of three-dimensionally ordered micromesoporous carbon

The 3DOmm carbon was prepared using SiO_2 nanoparticles as a hard template [51]. The SiO_2 nanoparticles were prepared in the compositional series of $150SiO_2$-1.2lysine-$9500H_2O$–600EtOH. The initial compounds (L-lysine, tetraethyl orthosilicate and deionized water) were mixed, followed by stirring at 500 rpm and a temperature of 363 K for 48 h. After this, removal of lysine-silica nanoparticle sols was carried out at 823 K for 12 h in a calcination oven (CLASIC Ltd.). The space between silica nanoparticles was filled with a carbon precursor (furfurylalcohol) and oxalic acid, at a ratio of 200/1. The mixture of SiO_2 particles with carbon precursor was placed in the calcination oven for carbon precursor polymerization at 363 K for 3 days. The calcined product was first heated in a tube furnace (CLASIC Ltd.) to the pyrolysis temperature of 473 K for

3 h, then to the carbonization temperature of 1173 K for 3 h at a heating rate of 3 K/min under a nitrogen flow of 100 ml/min. After carbonization, the product was added to a solution of 40% hydrofluoric acid for at least 24 h at room temperature to remove the SiO_2 nanoparticles. The resulting carbon was washed with deionized water, filtered and then dried. To confirm the complete removal of SiO_2, the 3DOmm carbon underwent ash content determination using the ISO 1171:2010 standard method (Solid mineral fuels — Determination of ash [52]). The analysis yielded no ash content, providing evidence for the absence of silica nanoparticles within the carbon network. Synthetic route of the carbon samples preparation using the SiO_2 nanoparticles as the hard template is shown in Fig. 1.

Physical activation of the post-synthesized 3DOmm carbon was carried out using CO_2 gas as the activating agent at temperatures of 973 K, 1073 K and 1173 K for 30 min in the tube furnace. Accordingly, the samples were marked as 3DOmm-973, 3DOmm-1073 and 3DOmm-1173, where the numbers correspond to the corresponding activation temperatures. The weight loss percentage of the 3DOmm carbon as a result of physical activation was in the range of ~3–5%, and it increased with increasing activation temperature.

2.3. Characterization of carbon materials

The ordered mesoporous structure of the prepared carbon materials was determined from small-angle X-ray scattering (SAXS) using a Xenocs Xeuss 2.0 SAXS instrument equipped with Cu Kα (λ = 0.15418 nm) radiation X-ray micro-focus sources, parallel beam point focus collimating system, and a Pilatus 200k (Dectris) hybrid pixel single-photon counting detector. The scattering vector (q) was calculated as $q = (4\pi/\lambda)\sin\theta$, where λ is the wavelength and 2θ is the scattering angle. Calibration of the primary beam position and distances from a sample to the detector was carried out using the AgBehenate powder sample. Measured 2D SAXS images were azimuthally integrated into 1D SAXS curves. The scattering from the sample holder was subtracted from measured data.

To evaluate the crystallographic properties of the prepared carbon samples, X-ray diffraction (XRD) was performed. The XRD patterns were measured using a Rigaku SmartLab diffractometer equipped with X-ray source, having Cu Kα radiation (λ = 0.15418 nm) of 9 kW power. High Pix-3000 2D hybrid pixel single photon counting detector was used to record the diffractograms, and s set of axial divergence eliminating soller slits with acceptance 5° in both incident and diffracted beam was applied.

To estimate disorder (i.e. the relative amount of crystallite boundaries) of the powder carbon samples, Raman spectroscopy was carried out using confocal Raman micro-spectrometer *alpha300 RSA* (WITec, Germany) with 633 nm He–Ne excitation laser. 50 × microscope objective (LD EC Epiplan-Neofluar, N.A. 0.55, Zeiss, Germany) was used to focus the 1 mW excitation laser to a diameter ~1.5 μm on the sample, and the single point spectra were integrated for 120 s (240 × 0.5 s, i.e. 2 min.). Spectra were collected using a 300 grooves/mm grating and thermoelectrically cooled CCD detector. The spectrometer was calibrated using Ar/Hg-glow lamp. The data were analysed using Project SIX Plus 6.0 software (WITec, Germany) to remove cosmic ray traces and background subtraction. Subsequent spectra normalization (at G-peak) and fitting were performed in Grams/AI 9.1 (Thermo Fisher Scientific Ltd., USA). To analyse I_D/I_G ratio, 10 spectra of each sample were used.

The morphology of the carbon samples was studied using a JEOL JEM 2200 high-resolution transmission electron microscope (HRTEM) operated at an accelerating voltage of 200 kV and a Mira 3 (Tescan) scanning electron microscope (SEM) operating at 30 keV electron beam energy.

The micropore and mesopore parameters of the carbon materials were determined using the adsorption technique. Accordingly, the ultramicropore parameters were evaluated from the CO_2 adsorption isotherms measured at 273 K using an IGA-100 gravimetric sorption analyzer (Hiden Isochema Ltd.). The CO_2 adsorption isotherms measured at p/p_s up to ~0.028 (the CO_2 saturation vapour pressure p_s ~3.5 MPa at 273 K) were fitted with the Dubinin-Radushkevich (DR) model [53] to determine the volume of narrow micropores (V_{micro}), and the Non-local density functional theory (NLDFT) model using the SAIEUS software from Micromeritics Ltd. to plot the pore size distribution in the narrow micropore range (<1 nm), and to evaluate the diameters of ultramicropores (d_{ultra}). The N_2 adsorption isotherms measured at 77 K using a SURFER volumetric sorption analyzer (Thermo Fisher Scientific Ltd.) were fitted with the Brauner-Emmet-Teller (BET) to determine the specific surface area (S_{BET}) and the NLDFT to obtain the pore size distribution in the range of supermicropores and mesopores (1–30 nm), and to estimate the diameters of micropores (d_{micro}) and mesopores (D_{meso}). The mesopore volume (V_{meso}) was

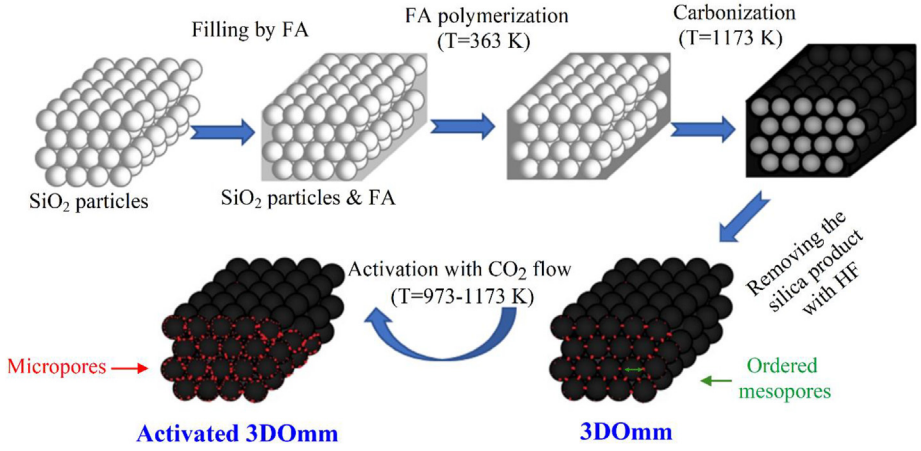

Fig. 1. Synthetic route of the activated 3DOmm carbons prepared using silica nanoparticles as a hard template, furfuryl alcohol (FA) as a carbon precursor and CO_2 gas as an activator.

calculated as the difference between the total pore volume (V_{tot}) estimated at $p/p_s = 0.98$ by the Gurvitch equation and the V_{micro} estimated from the NLDFT data.

2.4. CO_2 adsorption measurements

The CO_2 adsorption-desorption measurements were carried out on the carbon samples degassed at 433 K under a vacuum (10^{-6} kPa) overnight using an IGA-100 gravimetric sorption analyzer (Hiden Isochema Ltd.). A schematic representation of the IGA-100 is shown in our previous work [51]. The CO_2 adsorption-desorption isotherms were collected at low (up to 100 kPa) and higher (up to 2 MPa) pressures at different temperatures on about 30 mg of carbon. A time of 30 min was set for reaching equilibrium for each isotherm point in the measured pressure range, as well as for the adsorption-desorption cycles performed at 298 K and 100 kPa. The pressure accuracy was ±0.02%, and the temperature accuracy was ±0.05 K.

The CO_2 breakthrough curves were measured with the IGA-100 analyzer connected to the HRP-20 QIC quadrupole mass (Hiden Isochema Ltd.), which recorded the CO_2 concentration exiting the adsorption bed. The breakthrough curves, representing C/C_0 vs. time, where C is the outlet CO_2 concentration and C_0 is the inlet CO_2 concentration measured at time t, were recorded on a sample with a weight of ca. 20–30 mg under a dynamic gas mixture, containing 15 vol % of CO_2 and 85 vol % of N_2 at 298 K with a flow rate of 50 ml/min. A schematic representation of the experimental breakthrough measurements is shown in our previous study [44].

2.5. Kinetics of CO_2 adsorption

Pseudo-first order (PFO) [47] and pseudo-second order (PSO) models [54] were used to analyse the kinetics of the CO_2 adsorption. According to PFO (Eq. (1)), the adsorption rate is proportional to the number of adsorption sites, while the pseudo-second order (PSO) (Eq. (2)) assumes that the adsorption rate is proportional to the square of the number of adsorption sites.

$$q(t) = q_e\left(1 - e^{k_1 t}\right) \tag{1}$$

$$q(t) = \frac{q_e^2 k_2 t}{1 + q_e k_2 t} \tag{2}$$

where $q(t)$ and q_e are the amount of CO_2 adsorbed at time t and at equilibrium, respectively, and k_1 and k_2 are kinetic constants from PFO and PSO, respectively.

2.6. Selectivity of CO_2 over N_2

The determination of CO_2/N_2 selectivity (S_{CO_2/N_2}) was carried out using the Ideal Adsorbed Solution Theory (IAST) [55], where the data of pure CO_2 and N_2 adsorption isotherms were applied according to Eq. (3):

$$S_{CO_2/N_2} = \frac{x_{CO_2}/x_{N_2}}{y_{CO_2}/y_{N_2}} \tag{3}$$

where x_{CO_2} and x_{N_2} are the molar fraction of CO_2 and N_2, respectively, in the adsorbed phase, while y_{CO_2} and y_{N_2} are the molar fraction of CO_2 and N_2, respectively, in the bulk phase. The CO_2 and N_2 adsorption isotherms were measured with the IGA-100 gravimetric sorption analyzer. The N_2 gas used had a purity of 99.995 vol % (Linde Gas Ltd.).

2.7. Isosteric heats of CO_2 adsorption

Isosteric heats of CO_2 adsorption, as a function of the adsorbed amount at different temperatures, were estimated using the Clausius – Clapeyron Eq. (4).

$$ln\, p = -\left(\frac{\Delta H_{st}}{RT}\right) + C \tag{4}$$

where R is the ideal gas constant (8.315 J/K/mol), T is the absolute temperature, and C is a constant. Adsorption isosteres needed for calculating the isosteric heats were obtained using the Sips model.

3. Results and discussion

3.1. Characterization of the 3DOmm carbon materials

3.1.1. Ordered porous structure and morphology

SAXS profiles of the 3DOmm carbon samples are shown in Fig. 2. All studied samples show a sequence of intensive peaks with a first maximum at scattering vector magnitude q around of 0.027 Å^{-1} and consequent peaks at 0.044 Å^{-1}, 0.050 Å^{-1}, 0.068 Å^{-1} and 0.091 Å^{-1}. Considering a simplest model of close arrangement of solid spheres, it leads to the hexagonal close-packed (*hcp*) or face-centered cubic (*fcc*) stacking. A detailed inspection of peaks sequence and its intensities showed a periodic face center cubic arrangement of scattering objects.

A relevant physical model was developed for the SAXS data measured on 3DOmm samples: we assumed the spherical clusters of 3DOmm carbon having a mean size (Rc) and root mean square deviation of clusters radii (σRc). The clusters are filled with an ensemble of spherical bubbles arranged in the *fcc* lattice with centers of bubbles displaced by distance (D) and root mean square

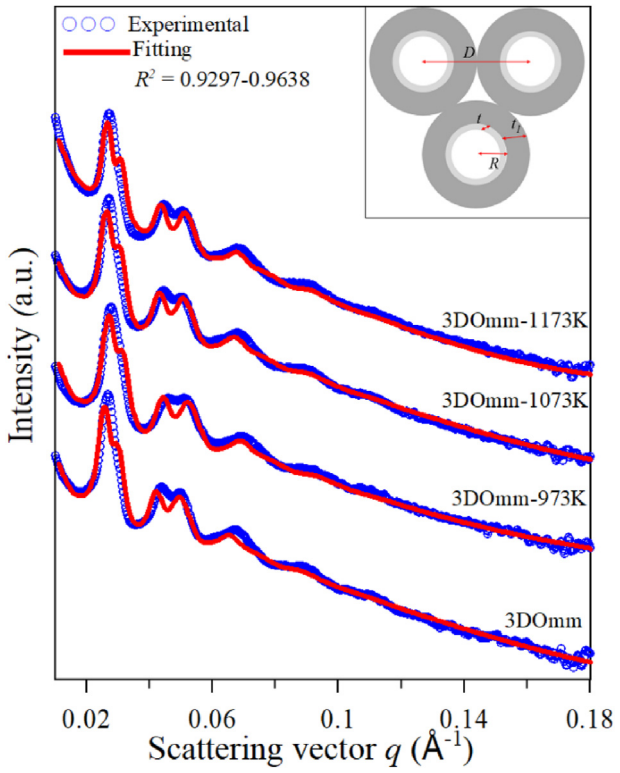

Fig. 2. Measured (open blue circles) and fitted (red lines) SAXS profiles of the 3DOmm carbon materials, and model used for the SAXS fittings (inset).

deviation (σD). Individual bubbles having an internal core-shell structure with radius (R), root mean square deviation (σR) and shell thickness (t). The SAXS intensity distribution is assumed as a weighted sum of intensities calculated using the decoupling (DA) and local monodisperse (LMA) approximations.

In all samples under study the mean cluster radius Rc lies around 280 nm. The mean distance of the bubbles centers D is around 28 nm, which represents the lattice parameter of the face centered cubic structure, calculated as $a = D\sqrt{2}$, around 40 nm. The mean bubble diameter (d) decreases from 18.26 nm in the 3DOmm sample to 9.72 nm in the 3DOmm-1173 K. The mean shell thickness (t) represents the fluctuations in densities or by the other words increasing porosity in the carbon walls (bubble interface), while the mean shell thickness (t_1) corresponds to the carbon wall according to the model shown as inset in Fig. 2.

As it is clearly seen in Fig. 2 the model pretty well describes/fits the measure data (compare the measured and fitted SAXS intensity profiles in Fig. 2). However still some deviations of the model from measured data are visible (the correlation coefficients R^2 = 0.9297–0.9638, being the lowest for the non-activated 3DOmm carbon and the best for the 3DOmm-973K). This is probably caused by fact that the model does not consider either the unorganized micro, or nanoporosity, or unorganized carbon atoms, which are usually present in carbon materials creating additional SAXS signal contribution. The refined values of the 3DOmm model are given in Table 1. Observation from the SAXS results indicated that the activation process of the 3DOmm carbon did not disrupt the ordered mesoporous structure of this carbon. With an increase in the activation temperature, the shrinkage of the thin carbon walls determined in the 3DOmm carbon was observed, which led to a decrease in the diameter of the ordered mesopores and formation of the thicker carbon walls (t_1) in the sample 3DOmm-1173K (Table 1).

The crystallographic structure of the prepared 3DOmm carbon samples measured by XRD (Fig. S1a) revealed one tiny broad peak at 2θ = ~18–28° characteristic for the (002) crystalline plane of graphitic carbon [56], indicating an amorphous structure of the 3DOmm carbons with a small graphitization. The Raman spectra measured on the 3DOmm carbons (Fig. S1b) were used to estimate disorder (i.e. the relative amount of crystallite boundaries) from estimation of the D- and G-peaks [15]. Accordingly, a broad peak at 1316 cm^{-1}, denoted as D-band, reflects breathing vibrations of C sp^2 atoms in rings and indicates the presence of disorder, distortions, and other crystal defects in the material. At the same time, the peak at 1589-1593 cm^{-1}, denoted as G-band, corresponds to the in-plane bond-stretching vibrations of pairs of C sp^2 atoms in graphitic structure [57]. The intensity ratios (I_D/I_G) determined in the range of 1.05–1.08 indicated the prevailing amorphous structure of the 3DOmm carbon samples [58]. It is also evident that the I_D/I_G values of the non-activated 3DOmm carbon and the 3DOmm-973K were similar, showing that the amount of disorder at an activation temperature of 973 K did not change. However, at activation temperatures above 973 K, the I_D/I_G values increased slightly, indicating that more destruction of the graphite structure occurred compared with the non-activated 3DOmm carbon. The growth of defects in carbon materials can be attributed to pore generation during the activation process, which leads to arbitrarily oriented graphitic carbon layers [56].

The HRTEM and the SEM images of the 3DOmm carbon samples at different magnifications are given in Fig. 3. This analysis was used to describe the morphology of the carbon samples. All carbon materials revealed a well-ordered structure composed of spherical bubbles of diameter about 25 nm. The physical activation of the initial 3DOmm carbon at different temperatures did not cause any visible destruction of the carbon structure. The observations from HRTEM and SEM images coincided well with the results obtained from the SAXS, where the mean distance of bubble centers, corresponding to the diameter of the entire spherical bubbles in the 3DOmm carbon materials was about 28 nm (Table 1). For a comparison of the morphology of the 3DOmm carbons with typical carbons, SEM images of commercial activated carbons marked as SH-PU 4.0 (Hübner sorbents) used for air purification and SC 40 (Silcarbon) used for air and water purification are shown in Fig. S2.

3.1.2. Microporous and mesoporous structure

The CO_2 adsorption isotherms, measured at a temperature of 273 K and relative pressures (p/p_s) of up to ~0.028 (saturation CO_2 vapour pressure p_s ~ 3.5 MPa at 273 K) were fitted with the Dubinin-Radushkevich adsorption model [53] to determine the volume of narrow micropores (V_{micro}) and with the NLDFT adsorption model to obtain the size distribution of the narrow micropores shown in Fig. 4a (cumulative pore volume as a function of narrow pores less than 1 nm is shown in Fig. S3a). The determined parameters are listed in Table 2. The non-activated 3DOmm carbon revealed the lowest V_{micro}, having 0.23 cm^3/g with the ultramicropore diameters $d1_{ultra}$ and $d2_{ultra}$ of 0.41 nm and 0.55 nm, respectively (narrow micropores less than ~0.7 nm are known as ultramicropores [22]). By subjecting this carbon to a CO_2 atmosphere for 30 min at 973 K, the ultramicropores of 0.41 nm were expanded over a wider range with a diameter of 0.46 nm in the 3DOmm-973K, occupying the volume of 0.27 cm^3/g. The micropore volume value obtained for the 3DOmm-973K sample was the highest obtained amongst all activated 3DOmm carbons. With increasing activation temperature above 973 K, the micropore volume decreased, depending on the activation temperature similar to mesopore and micropore volumes (Table 2). However, the diameters of the ultramicropores in the 3DOmm-1073K and 3DOmm-1173K remained the same as those of the initial non-activated 3DOmm sample.

The N_2 adsorption-desorption isotherms measured on the carbon samples at a temperature of 77 K were used to plot the BJH pore size distribution in the range of mesopores (2–50 nm) shown in Fig. 4b (cumulative pore volume as a function of pore size can be seen in Fig. S3b). The measured N_2 sorption isotherms showed a type IV shape with a type H1 hysteresis loop typical for cylindrical mesopores in a narrow distribution range [59] (Fig. S4). The type IV

Table 1
Parameters of the 3DOmm carbons obtained from the fitting of the SAXS profiles.

Sample	Rc (nm)	σRc	D (nm)	a (nm)	σD	R (nm)	σR	d (nm)	t (nm)	t_1 (nm)
3DOmm	374.1	2.86	28.6	40.5	2.22	9.13	1.65	18.26	2.53	2.64
3DOmm-973K	279.9	2.26	27.9	39.6	2.23	6.05	5.53	12.01	2.33	5.57
3DOmm-1073K	276.1	2.27	28.8	40.7	2.27	6.38	5.46	12.76	2.32	6.62
3DOmm-1173K	286.7	2.11	28.5	40.3	2.06	4.86	4.09	9.72	2.76	7.40

Rc is mean cluster radius, σRc is rmc of the mean cluster radius, D is mean distance of bubble centers, a is lattice parameter, σD is rmc of mean distance of bubble centers, R is mean bubble radius, σR is rmc of the mean bubble radius, d is mean bubble diameter, t is porosity thickness, t_1 is wall thickness.

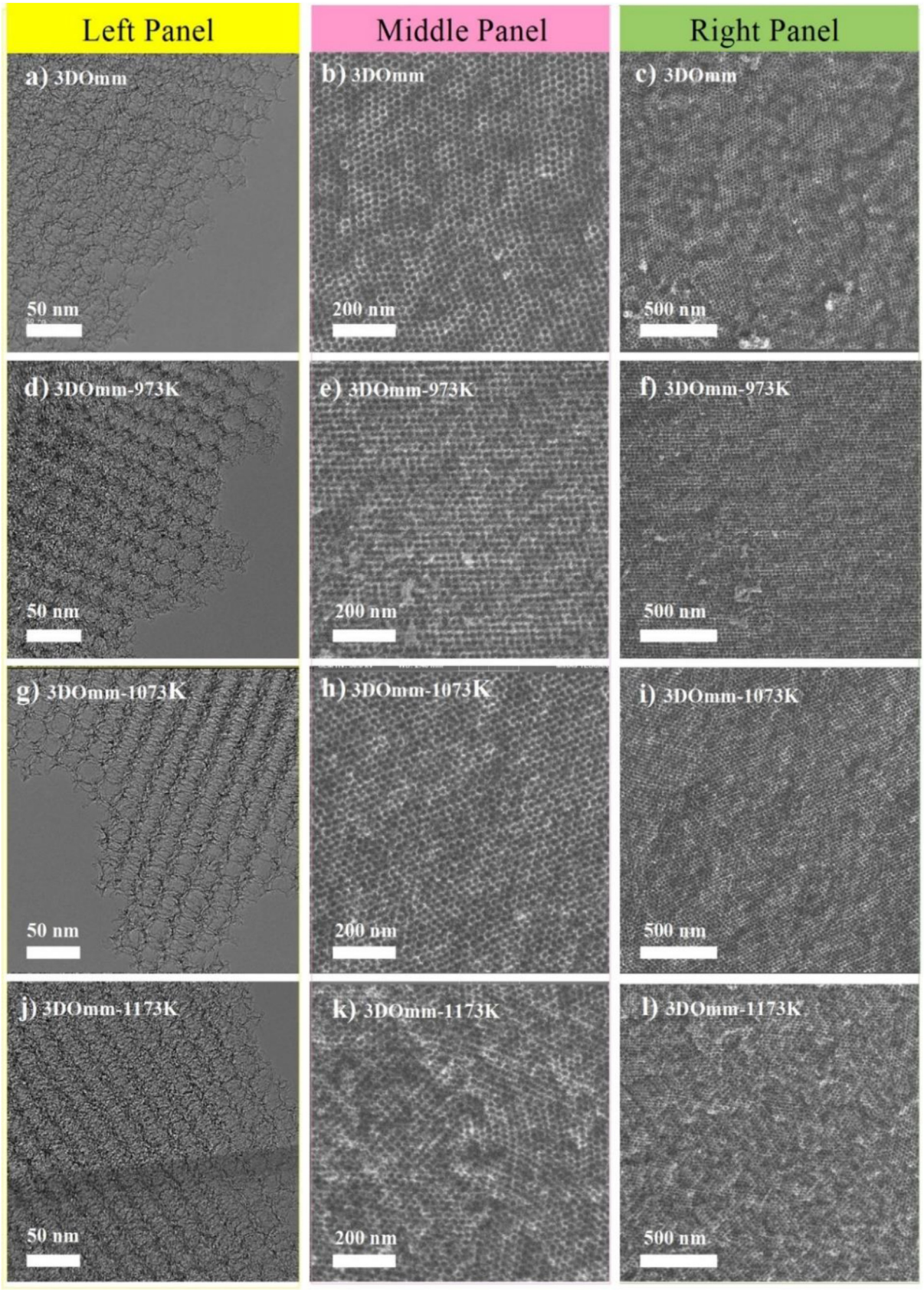

Fig. 3. The left panel displays HRTEM images at a scale bar of 50 nm, the middle panel shows SEM images at a scale bar of 200 nm, and the right panel shows SEM images at a scale bar of 500 nm obtained on a-c) 3DOmm, d-f) 3DOmm-973K, g-i) 3DOmm-1073K and j-l) 3DOmm-1173K carbon samples.

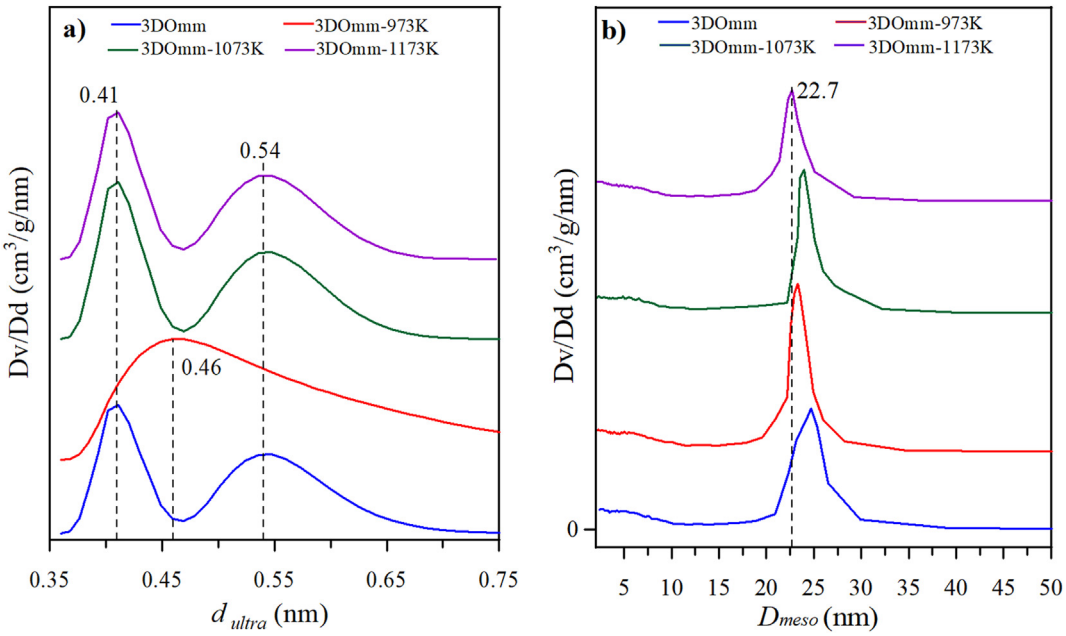

Fig. 4. Pore size distribution obtained from the a) NLDFT applied to the CO_2 adsorption isotherms measured at 273 K and b) BJH applied to the N_2 adsorption isotherms at 77 K.

Table 2
Pore parameters of the 3DOmm samples.

Sample	CO_2 adsorption at 273 K			N_2 adsorption at 77 K			
	V_{micro}	$d1_{ultra}$	$d2_{ultra}$	V_{meso}	D_{meso}	V_{tot}	S_{BET}
	(cm^3/g)	(nm)	(nm)	(cm^3/g)	(nm)	(cm^3/g)	(m^2/g)
3DOmm	0.23	0.41	0.55	3.70	24.7	3.79	1058
3DOmm-973K	0.27	0.46	–	3.94	23.3	4.20	1462
3DOmm-1073K	0.25	0.41	0.55	3.42	24.0	3.64	1256
3DOmm-1173K	0.24	0.41	0.55	2.75	22.7	2.91	1052

CO_2 adsorption at 273 K: V_{micro} from DR; $d1_{ultra}$ and $d2_{ultra}$ from NLDFT.
N_2 adsorption at 77 K: $V_{meso} = V_{tot}$-V_{micro}; V_{tot} from Gurvich at $p/p_s = 0.99$; D_{meso} from BJH; S_{BET} from BET.

shape also indicated the presence of abundant micropores at a relative pressure less than 0.02 [60]. The shapes and hysteresis loops of N_2 adsorption-desorption isotherms obtained on the 3DOmm carbons were in good agreement with the results obtained on a similar carbon type published in our previous work [51]. In the mesopore region, the BJH pore size distribution for the carbons revealed an intense peak within the range of ~20–30 nm with a maximum, corresponding to the mesopore diameter (D_{meso}), laying within the range of 22.7–24.7 nm (Fig. 4b, Table 2). The mesopore diameters coincided well with the SEM analysis (see Fig. 3). The activation procedure of the post-synthesized 3DOmm carbon had a considerable impact on the BET specific surface area (S_{BET}) and mesopore volumes (V_{meso}). Accordingly, activating it at a temperature of 973 K led to an increase of the S_{BET} value from 1058 m^2/g (in the post-synthesized 3DOmm carbon) to 1462 m^2/g (in the activated 3DOmm-973K carbon), and the mesopore volume increased from 3.70 cm^3/g to 3.94 cm^3/g, respectively. However, with a further increase in activation temperature, these parameters decreased.

It is known that an increase in activation temperature causes a more intense interaction of CO_2 molecules with the carbon surface, which can lead to the creation of new micropores in the carbon walls and widening of already existing pores [61,62]. The results obtained here indicate that activation of the 3DOmm carbon at 973 K leads to additional microporosity together with broadening of existing mesopores, causing an increase in the microporous and mesoporous volumes. However, it was apparent that increasing activation temperature above 973 K caused the decrease of the volume of the micropores possibly due to growth of existing micropores in the very thin carbon walls of about 2.64 nm in the 3DOmm carbon (see Table 1) to the size of small mesopores, leading to decreased microporosity (i.e. micropore volume) and S_{BET} values. As the SAXS results showed, shrinkage of the thin carbon walls in the 3DOmm carbon with the increased activation temperature occurred, leading to a thickening of the carbon walls and a decrease in the diameter of the ordered mesopores in the activated 3DOmm carbons (Table 1, Fig. 2). Thus, smaller ordered mesopores occupied smaller volumes. In addition, expansion of some mesopores to macropores, which cannot be determined from the adsorption isotherm, influencing the decrease of the mesopore volume with the activation temperature could also take place.

3.2. CO_2 adsorption performance

3.2.1. CO_2 adsorption capacities

The CO_2 adsorption performances of non-activated and activated 3DOmm carbon materials were evaluated from measurements of CO_2 adsorption capacities at atmospheric (100 kPa) and higher (up to 2 MPa) pressures and at different temperatures.

In addition to the CO_2 adsorption measurements performed at 273 K and pressures within the range of 0–100 kPa, CO_2 adsorption isotherms were also measured at 298 and 323 K. These adsorption and desorption isotherms are shown in Fig. 5. The desorption isotherms exhibited a significant overlap with their respective adsorption isotherms, indicating a high degree of reversibility for the 3DOmm carbon samples. Due to the strong overlap between the desorption and adsorption isotherms, the desorption curves may not be clearly distinguishable in some instances in Fig. 5. The CO_2 adsorption capacities of all carbon materials were dependent on temperature, i.e. they decreased as the temperature increased, due to the increase in molecular kinetic energy of CO_2 with temperature [63]. The CO_2 adsorption capacity at a pressure of 100 kPa was found to be in the range of 2.71–3.19 mmol/g at 273 K (Figs. 5a),

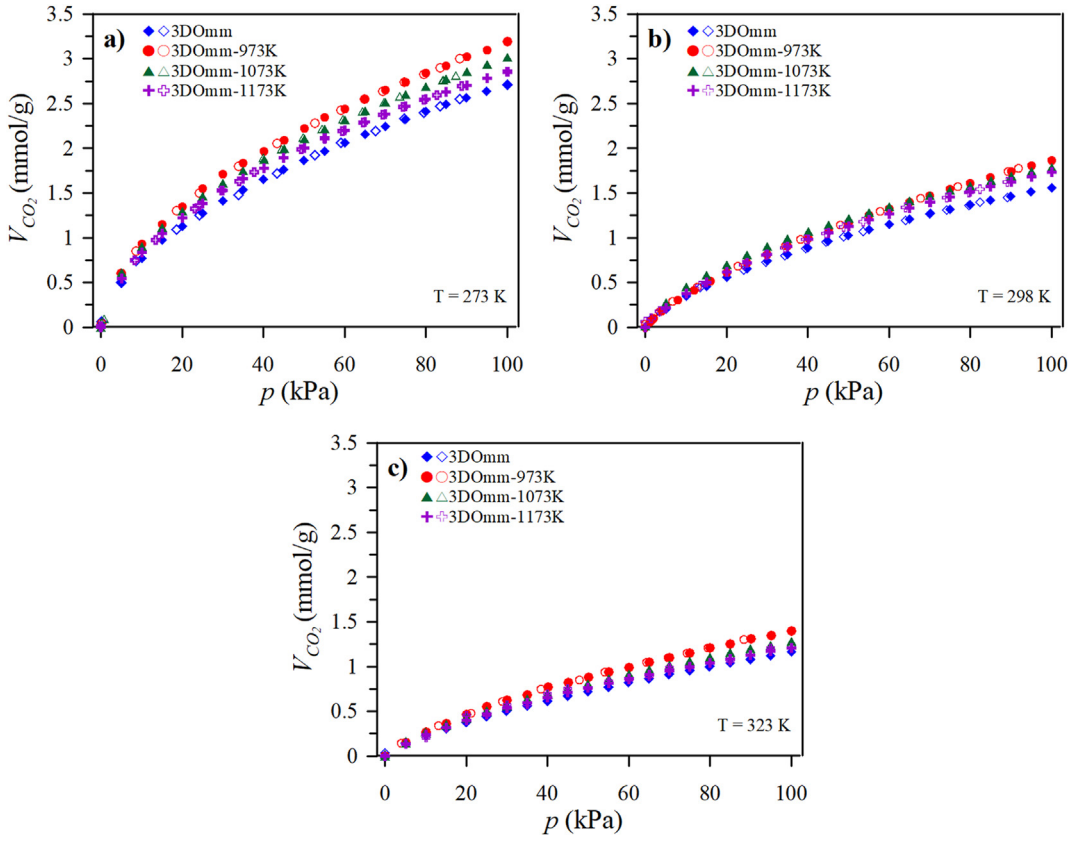

Fig. 5. CO_2 adsorption isotherms measured at 100 kPa on carbon samples at different temperatures: a) 273 K, b) 298 K and c) 323 K. The bold symbols correspond to the adsorption isotherm, and the empty symbols correspond to the desorption isotherm.

1.56–1.87 mmol/g at 298 K (Figs. 5b) and 1.16–1.40 mmol/g at 323 K (Fig. 5c). The initial non-activated 3DOmm carbon revealed the lowest adsorption performance at each measured temperature, while by activating the 3DOmm carbon at 973 K, the CO_2 adsorption capacity was significantly enhanced, showing the highest adsorption capacity amongst all the activated carbons.

The CO_2 adsorption and desorption isotherms measured on the carbon samples at 298 K, 308 K and 323 K and pressures up to 2 MPa are shown in Fig. 6a–c, respectively. At 2 MPa, the 3DOmm-973 K carbon also revealed the highest CO_2 adsorption performance, adsorbing 11.18 mmol/g at 298 K, 9.98 mmol/g at 308 K and 7.70 mmol/g at 323 K. In contrast to the atmospheric pressure, the activated 3DOmm-1173K carbon adsorbed the smallest amount of CO_2 among all carbons studied (7.21 mmol/g at 298 K, 6.4 mmol/g at 308 K and 5.43 mmol/g at 323 K). As in the case of atmospheric pressure, exothermic adsorption was observed.

Variations in adsorption capacity in the carbon materials at different pressures are attributed to the number of micropores and mesopores present in their structure. The effect of porosity on the CO_2 adsorption properties of carbon materials has been widely described [20,38]. Two processes influence adsorption in micropores - the filling mechanism and surface coverage [51]. During CO_2 adsorption in micropores, both these processes are related to the kinetic diameter of the CO_2 molecule (0.33 nm) and micropore size. The surfaces of narrow micropores with widths below 0.6 nm have very strong Van der Waals interactions with CO_2 molecules, leading to the filling mechanism. However, if the micropore size is greater than 0.6 nm, corresponding to about two CO_2 molecular dimensions, then the coverage CO_2 adsorption mechanism takes place [21]. For high adsorption of the CO_2 at atmospheric pressure, the requirement of narrow micropores was considered [22,64].

For the carbon samples studied, the CO_2 adsorption capacity of 1.56 mmol/g determined in the 3DOmm carbon with a micropore volume of 0.23 cm^3/g increased to 1.87 mmol/g in 3DOmm-973 K with a micropore volume of 0.27 cm^3/g, both at atmospheric pressure (Table 2, Fig. 5). In contrast, an increase in volume of bigger micropores and mesopores led to an increase in adsorption capacity at higher pressures. The 3DOmm-1173K carbon with mesopore volume of 2.75 cm^3/g adsorbed the lowest amount of CO_2 of 7.21 mmol/g, and the 3DOmm-973 K, comprising a mesopore volume of 3.94 cm^3/g showed the highest adsorption capacity of 11.26 mmol/g at 2 MPa (Table 2, Fig. 6). The changes in adsorption capacity with pressure obtained on the 3DOmm carbon samples are in good agreement with the theory of micropore filling of CO_2 at low pressures [34,65] and mesopore filling of CO_2 at higher pressures [19].

The experimental CO_2 adsorption isotherms measured up to 2 MPa were fitted with the Sips adsorption model, which combines the Langmuir and Freundlich adsorption models to study the adsorption process on the 3DOmm carbon materials [47]. According to the Langmuir model, monolayer adsorption takes place, assuming that the molecules do not interact amongst themselves and each molecule occupies the one adsorption site (homogeneous adsorption). On the contrary, the Freundlich model is not limited to monolayer adsorption. Therefore, it can be applied to multilayer adsorption, determining the exponential distribution of adsorption sites and their energies (heterogeneous adsorption) [66]. Thus, in the case of the Sips equation, the exponent *n*, being in the range of

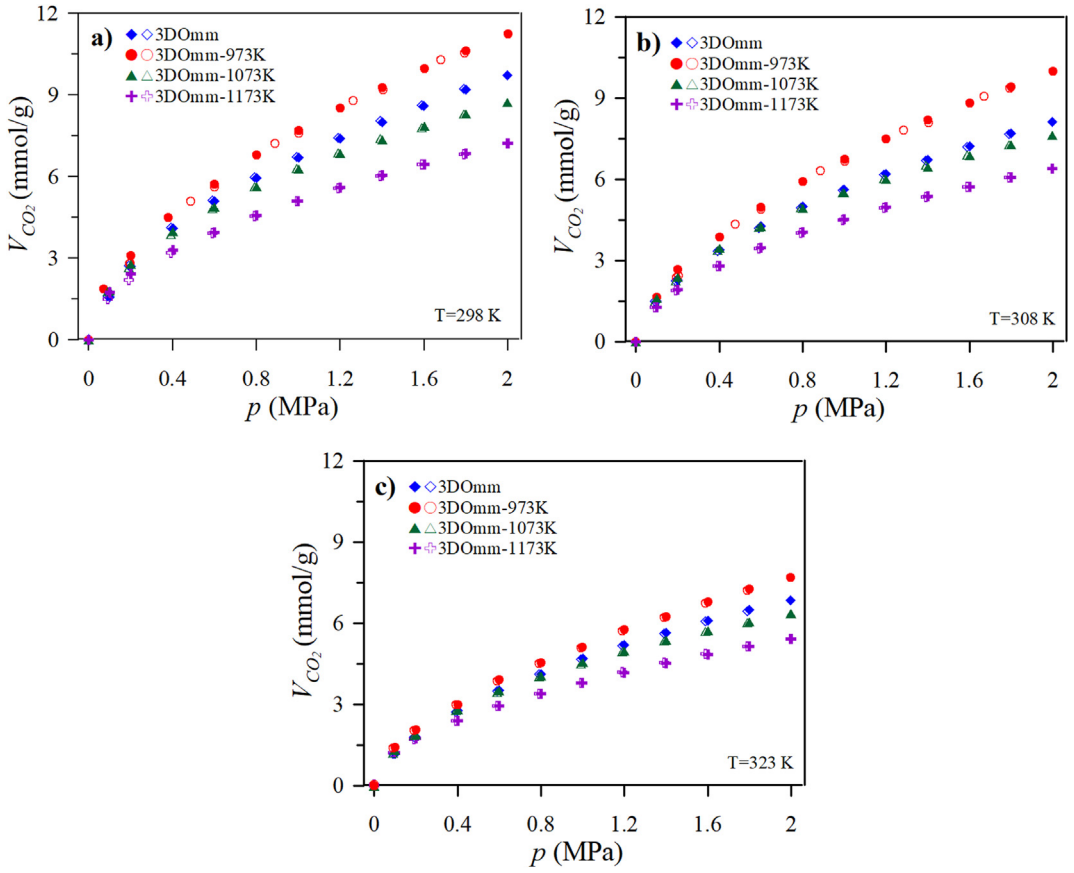

Fig. 6. CO_2 adsorption isotherms measured on 3DOmm carbon samples at 2 MPa at different temperatures: a) 298 K, b) 308 K, c) 323 K. The bold symbols correspond to the adsorption isotherm, and the empty symbols correspond to the desorption isotherm.

0–1, shows the degree of heterogeneity. When $n = 1$, then the Sips equation turns into the Langmuir equation, describing homogeneous adsorption. The fittings of experimental adsorption isotherms measured at pressures up to 2 MPa and different temperatures with the described adsorption model are shown in Fig. 7a–d. The adsorption model showed very good fitting results, having correlation coefficients (R^2) close to 1. The parameters calculated for the Sips model are summarised in Table 3. Since the exponent n is in the range of 0.57–0.70, it was assumed that the heterogeneous adsorption mechanism on the 3DOmm carbon surfaces prevailed when CO_2 adsorption occurred at pressures up to 2 MPa. The heterogeneous CO_2 adsorption observed on the 3DOmm carbons can be explained by the variety of pore sizes in the micromesoporous carbon materials, i.e. first the micropores are filled with CO_2 at low pressures, and then the mesopores at higher pressures [19].

The CO_2 adsorption capacities of the 3DOmm-973K carbon, which showed the best CO_2 adsorption performance, were compared with the adsorption capacities observed on different carbon-based materials and are given in Table 4. At atmospheric pressure, the carbon samples containing higher micropore volumes showed higher CO_2 adsorption performance compared to those with lower micropore volumes [17,21,23,24,26,38,49–51]. High microporosity in the carbon materials was obtained primarily due to various activating agents, such as KOH [19,21–24,29,46,68,69], K_2CO_3 [34] and $K_2C_2O_4$ [30]. Especially, an extremely high CO_2 uptake of 9.05 mmol/g at 273 K was reported by the activated carbons prepared from the common polypody as a feedstock due to a large volume of micropores [23]. However, nanoporous carbon materials published in Ref. [19] showed a controversial trend with micropores and mesopores, i.e. a fairly low adsorption performance at 100 kPa despite having a high volume of micropores, and very high adsorption capacity at 2 MPa despite having a small mesoporous volume compared to the 3DOmm carbons studied in this work and previously studied by us [51]. The carbon samples containing functionalities in their structure also declined from the trend of CO_2 depending on the micropore volume at low pressures since the different functionalities enhanced the CO_2 adsorption [22,29,43,70,71]. Accordingly, heteroatom (N, S, O) doping of carbons showed a positive effect on CO_2 capture performance due to Lewis acid-base interactions between pyrrolic/pyridinic nitrogen and CO_2 molecules, and strong energy interactions between oxidized sulfur atoms and CO_2 molecules [30,46]. The CO_2 adsorption at 2 MPa (a relative pressure p/p_s ~0.31 at 298 K) showed a dependence on mesopore volume in the case of pure non-doped carbons such as 3DOmm carbon [51] and mesoporous CMK-3 and FCMK-3 carbons [25]. However, the microporous carbon (G-850-5) and the micromesoporous carbon (G-3.6–2) [24], having a smaller mesopore volume compared with 3DOmm carbons, showed higher adsorption performance of CO_2 at 2 MPa. According to the authors suggestion [24], the G-850-5 and G-3.6–2 carbon materials comprised the large volume of pores less than 2.0–2.4 nm, leading to high adsorption performance in carbon materials containing bigger mesopore volumes.

3.2.2. CO_2/N_2 selectivity

In the case of the post-combustion capture, a typical flue gas contains a low level of CO_2 (~15 vol %) and a large amount of N_2

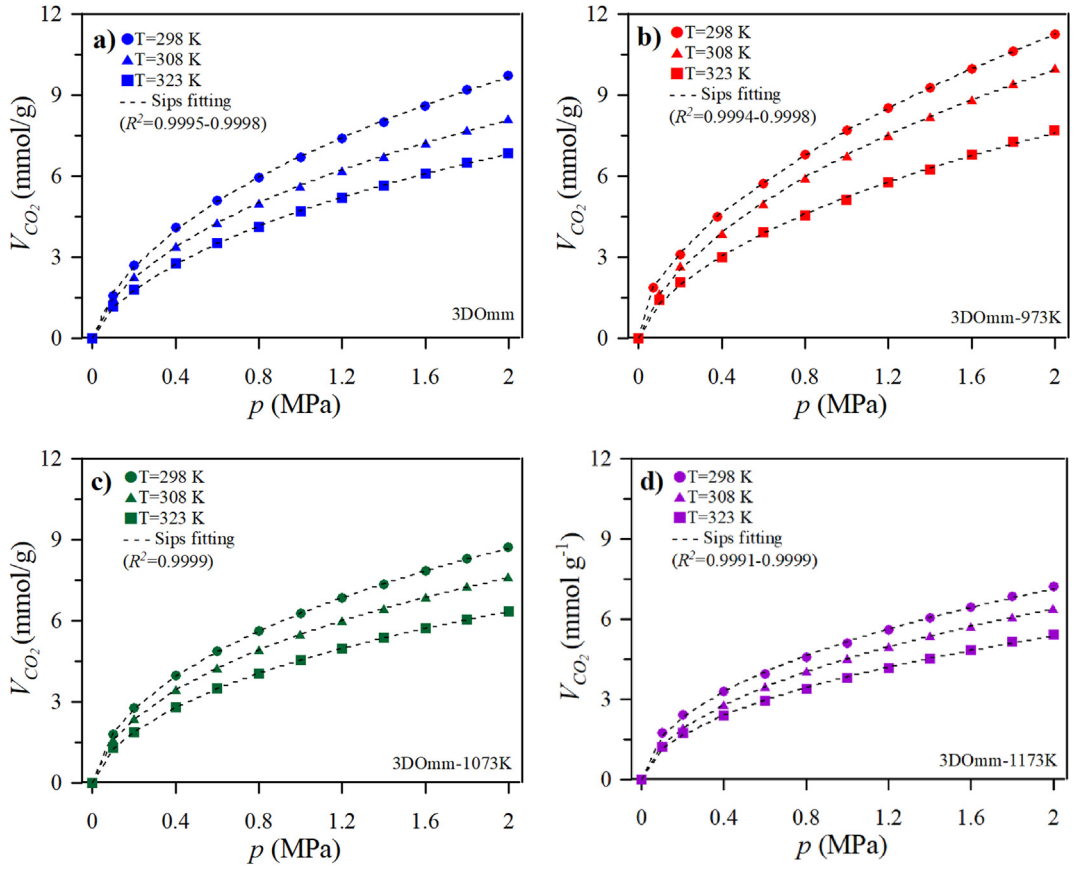

Fig. 7. CO_2 adsorption isotherms and their fittings with the Sips model obtained on the a) 3DOmm, b) 3DOmm-973 K, c) 3DOmm-1073 K and d) 3DOmm-1173 K carbon materials at different temperatures.

Table 3
Results from Sips fittings of the adsorption isotherms measured at different temperatures and pressures up to 2 MPa.

Sample	298 K				308 K				323 K			
	V_m	k	n	R^2	V_m	k	n	R^2	V_m	k	n	R^2
3DOmm	38.39	0.0961	0.6604	0.9995	29.29	0.1164	0.6664	0.9998	23.46	0.1404	0.7027	0.9998
3DOmm-973K	58.21	0.0547	0.6476	0.9998	43.05	0.0854	0.6812	0.9998	30.26	0.1004	0.6812	0.9994
3DOmm-1073K	35.51	0.0742	0.5913	0.9999	26.40	0.1148	0.6169	0.9999	21.32	0.1304	0.6410	0.9999
3DOmm-1173K	29.41	0.0668	0.5704	0.9991	20.81	0.1397	0.6474	0.9999	16.91	0.1456	0.6316	0.9992

V_m is maximum adsorption capacity (mmol/g), k is Sips isotherm model constant, n is Sips isotherm model exponent, R^2 is the correlation coefficient.

(~85 vol %) [10]. Due to the low partial pressure of CO_2, the estimation of selectivity of CO_2 towards N_2 in the binary gas mixture is very important. The CO_2/N_2 selectivity can be determined from data of the pure CO_2 and N_2 adsorption isotherms according to Eq. (3) based on IAST theory [72].

The pure CO_2 and N_2 adsorption isotherms measured on the 3DOmm carbon samples at pressures of up to 100 kPa and a temperature of 298 K are shown in Fig. 8a. Using the data of the CO_2 and N_2 adsorption isotherms, we calculated the CO_2/N_2 selectivity (S_{CO_2/N_2}) of the 3DOmm carbon samples for the gas mixture with a volume ratio of 15:85 according to Eq. (3). The dependence of the S_{CO_2/N_2} values on the pressure at 298 K are shown in Fig. 8b. At 5 kPa, the highest value of 119 was determined for 3DOmm, while the lowest selectivity was 41.4 in the 3DOmm-1173K. Selectivity then decreased with pressure over the entire pressure range for the three 3DOmm, 3DOmm-1073K and 3DOmm-1173K carbon samples. The last activated carbon, i.e. the 3DOmm-973K carbon, showed a slight increase in selectivity with pressure up to 16–20 kPa. However, a further pressure increase led to a slow decrease in selectivity (Fig. 8b). At 100 kPa, the CO_2/N_2 selectivity was in the range of 33.2–51.5. Within the pressure range above 40 kPa, the activated 3DOmm-973K carbon showed the highest selectivity, while the non-activated 3DOmm carbon was the worst carbon for selection of CO_2 from the binary CO_2–N_2 gas system.

The difference in the S_{CO_2/N_2} values at 5 kPa is due to the fact that the CO_2 is filled in the narrowest ultramicropores at low pressures [73], while the N_2 gas requires a little wider micropores due to higher kinetic diameter [51]. The 3DOmm carbon revealed the highest amount of the narrow micropores amongst the studied carbon materials (Table 2), and therefore it could capture higher amount of CO_2, reflecting in the highest selectivity value. On the contrary, the 3DOmm-973K carbon revealed the wider ultramicropores than the other carbon materials, and therefore this carbon adsorbed the smallest CO_2 amount at pressures up to 5 kPa. However, the best selectivity of 3DOmm-973K carbon at 100 kPa can be attributed to its highest microporosity compared to other

Table 4
Comparison of CO_2 adsorption capacities of initial non-activated 3DOmm carbon and activated at 973 K (3DOmm-973K) with the reported carbon materials.

Sample	Activating agent	Conditions (Temp; Pressure)	CO_2 adsorption	Specific surface area (S_{BET})	Micropore volume (V_{micro})	Mesopore volume (V_{meso})	Reference
			(mmol/g)	(m^2/g)	(cm^3/g)	(cm^3/g)	
3DOmm-973K	CO_2	273 K; 100 kPa 298 K; 100 kPa 298 K; 2 MPa	3.19 1.87 11.26	1462	0.27	4.03	This work
3DOmm	Non	273 K; 100 kPa 298 K; 100 kPa 298 K; 2 MPa	2.71 1.56 8.12	1058	0.23	3.72	This work
3DOmm	Non	298 K; 100 kPa 298 K; 2 MPa	1.49 9.12	1343	0.17	3.42	[51]
N-doped ordered mesoporous carbon (N-CMK-3_900)	Non	273 K; 100 kPa	~3.34	667	0.16	0.84	[33]
Halloysite-derived carbon	$ZnCl_2$	298 K; 2 MPa	~18	1646	0.43	1.29	[14]
Composite-derived carbons (C_ZIF-8)		303 K; 100 kPa 303 K; 1 MPa	~2.5 ~7.0	1862	0.65	0.01	[20]
Nanoporous carbons	KOH	298 K; 100 kPa 298 K; 2 MPa	~2.5–3.8 ~13–22	1770–3575	0.70–1.06	0.03–0.71	[19]
Microporous carbon spheres	KOH	273 K, 100 kPa	5.96–6.35	831–986	–	–	[21]
	Non	273 K, 100 kPa	3.51–3.78	462–486	–	–	
N-doped carbon (CUK-113)	KOH	273 K; 100 kPa 298 K; 100 kPa	6.37 3.91	2150	0.43	0.49	[22]
Nanoporous carbons (NCs)	KOH	273 K; 100 kPa	~4.00–9.05	187–1994	0.14–0.92	0.02–0.23	[23]
Microporous carbon (G-850-5)	KOH	298 K; 100 kPa 298 K; 2 MPa	4.5 ~12	1690	0.67	0.05	[24]
Micromesoporous carbon (G-3.6–2)	KOH	298 K; 100 kPa 298 K; 2 MPa	1.5 ~22	3460	1.00	1.72	
Mesoporous carbons (CMK types)	Non	298 K; 100 kPa 298 K; 2 MPa	~2.2 ~8.5–9.6	1258–1491	–	–	[25]
N,O-doped micromesoporous carbons	KOH	273 K; 100 kPa 298 K; 100 kPa	6.24–8.59 4.05–6.06	1266–2013	0.47–0.75	0.22–0.42	[29]
Activated carbons	K_2CO_3	273 K; 100 kPa	~3.11–4.2	2750–2910	1.33–1.47	0.44–0.51	[34]
N,O-doped carbon (PHC4)	$ZnCl_2$	273 K; 100 kPa 298 K; 2 MPa	3.5 ~13	1080	0.16	0.43	[43]
Activated CNFs	CO_2	298 K; 100 kPa	0.38–1.21	201–413	–	–	[60]
N-doped mesoporous carbons	at 373 K	273 K; 100 kPa 298 K; 100 kPa	2.84–3.40 1.32–1.63	491–610	0.24	0.15	[67]
Activated mesoporous carbons	KOH	298 K; 100 kPa	2.9–3.2	1200–2660	0.48–1.03	0.16–0.35	[68]
Microporous walnut shell-based carbons:	KOH	273 K; 100 kPa 273 K; 2 MPa	~3.16–3.55 ~8.3–9.6	1982–2497	0.57–0.64	0.02–0.13	[69]
N, S, O-doped activated carbons	KOH	273 K; 100 kPa 298 K; 100 kPa	2.37–5.38 1.64–3.57	430–2095	0.27–1.26	0.05–0.55	[46]
N-doped activated carbons (OPMKs)	$K_2C_2O_4$	273 K; 100 kPa 298 K; 100 kPa	3.16–6.67 1.86–3.97	1830–2130	0.96–1.12	1.11–1.20	[30]
N-doped mesoporous carbons	Non	298 K; 100 kPa	2.43–2.53	514–540	–	–	[70]
Carbon nanofibers:	Non	273 K; 100 kPa	4.63–5.08	990–1084	0.44–0.49	0.57–0.67	[71]

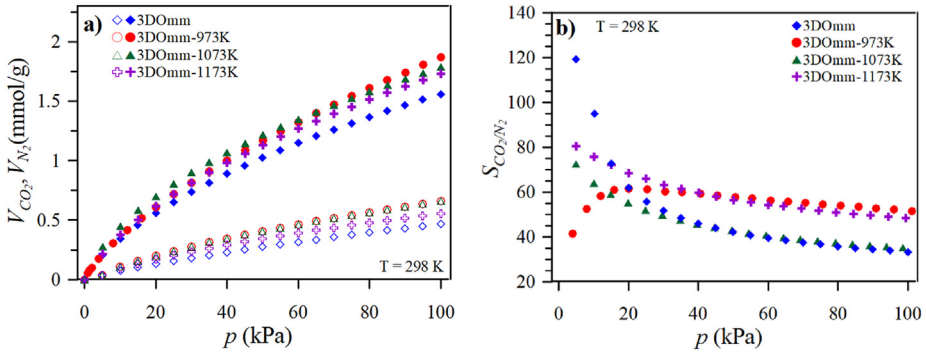

Fig. 8. a) CO_2 and N_2 adsorption isotherms and b) CO_2/N_2 selectivity for a volume ratio of 15:85 depending on different pressures up to 100 kPa at 298 K for all samples measured.

3DOmm carbon materials. At the same time, the 3DOmm carbon with the poorest microporosity exhibited the worst selectivity of CO_2 towards N_2. The selectivity of the 3DOmm-973K carbon was higher than the selectivity obtained on many other carbon-based materials for a gas mixture with a volume ratio of 15:85 at 298 K and 100 kPa [74,75].

To show how 3DOmm carbon materials capture CO_2 under post-combustion capture conditions, a dynamic sorption experiment was performed with a CO_2–N_2 gas mixture, keeping a volume ratio of CO_2:N_2 = 15:85 and a flow rate of 50 ml/min. Breakthrough curves obtained on the 3DOmm carbon materials at 298 K (Fig. S5) showed that the CO_2 uptake of the 3DOmm carbon materials ranged from 0.29 to 0.38 mmol/g. Notably, 3DOmm-973K carbon exhibited the highest performance among all the tested materials. The breakthrough of the 3DOmm carbon samples occurred at 0.91–1.51 min, considering the breakout time at $C/C_0 = 0.05$ [76]. The breakthrough time is directly proportional to the mass of the sample, and the sample amount used for the breakthrough experiments was only 20–30 mg, due to the limitations of the analyzer. The recorded breakthrough time was therefore relatively short compared to the published carbons [76–78]. To overcome this limitation and to gain a deeper understanding of the breakthrough behaviour with larger sample masses, we conducted breakthrough time calculations for each carbon sample using an amount of 1 g, resulting in breakthrough times ranging from 40.9 to 58.5 min. These breakthrough times exceeded those of amine-doped commercial activated carbons, which exhibited a slightly longer breakthrough time of 61.5 min. However, the amine-doped activated carbons required 3–6 times greater amounts of sorbent than our samples [79], and chemically activated nanoporous carbon with a breakthrough time of 3.15 min required an adsorbent weight of 2 g [56], etc. Moreover, a previous investigation [76] has revealed that the flow rate plays a pivotal role in both adsorption capacity and breakthrough time. At the lowest flow rate, the adsorption capacity was found to be highest, and the breakthrough time was longest, suggesting that a low flow rate is optimal for efficient CO_2 capture from a flue gas. It was also observed that a higher occupation of adsorption sites by N_2 molecules occurs during the initial stages of the breakthrough experiments. However, as the experiment progressed, the N_2 molecules were replaced by CO_2, leading to higher selectivity [56].

3.2.3. CO_2 adsorption kinetics

To analyse the kinetics of the dynamic CO_2 adsorption, the change in weight over time during the breakthrough experiment at 298 K shown in Figs. S6a–d was analysed. It was found that 95% of the adsorption saturation occurs within first 6.1–9.3 min. This is comparable with self S-doped porous carbon [80], and is considered to be fast adsorption kinetics. Fast adsorption kinetics is very important for practical applications.

To investigate the kinetics of CO_2 adsorption, we also analysed the change in weight over time during the pressure step from 0 to 100 kPa at 298 K under equilibrium conditions. As the carbon samples are lightweight and could potentially be blown out of the device, we adopted a cautious approach by using a slow pressure increase of 10 kPa per minute. However, this means that it could be challenging to evaluate the time of saturation accurately, due to the extended duration of the pressure increase. To overcome this limitation and to obtain a reliable understanding of the adsorption kinetics, we employed the pseudo-first order (PFO) model (Eq. (1)) [47] and the pseudo-second order (PSO) model (Eq. (2)) [54] for fitting the kinetics data. By comparing the results obtained from both models, we estimated the kinetics constants, providing valuable insights into the adsorption kinetics of CO_2 on the carbon samples. Fig. S7 illustrates the model fittings and their residuals, and Table 5 lists the values of the kinetic constants (k_1 and k_2), the correlation coefficients (R^2) and the root-mean-square deviation (*RMSE*) of the two models used for all carbon samples. Notably, the pseudo-first order model demonstrated superior fittings, as indicated by higher R^2 and lower *RMSE* values, suggesting that physical adsorption of CO_2 occurs. Furthermore, when comparing the carbon samples, we observed that the kinetic constant (k_1) was largest in the sample with the least CO_2 adsorption, namely 3DOmm-1173K. Interestingly, the value of k_1 decreased as the CO_2 adsorption amount increased across the samples. This trend can be attributed to the partial saturation as the available active sites on the carbon surface gradually become occupied by CO_2 molecules with increased CO_2 uptake. As a result, the rate of CO_2 adsorption starts to slow down, leading to a decrease in the kinetic constant [81]. This saturation effect occurs because the surface sites become less accessible to additional CO_2 molecules, reducing the overall rate of adsorption. Also, the slower diffusion rates of the CO_2 molecules through the gas phase towards the adsorption sites on the carbon surface can lead to a decrease in the kinetic constant (k_1) [82].

3.2.4. Interaction strength between CO_2 gas and carbon surfaces

The interaction strength between the CO_2 gas and carbon surface was evaluated from performing the CO_2 adsorption-desorption cycles on the 3DOmm carbons at 298 K and 100 kPa (Fig. 9a) and estimating the isosteric heats of CO_2 adsorption (ΔH_{st}) calculated as a function of the amount adsorbed at different temperatures using the Clausius – Clapeyron Eq. (4) (Fig. 9b).

Adsorption-desorption cycles with CO_2 performed on all 3DOmm carbon samples at 298 K and 100 kPa shown in Fig. 9a revealed that all samples exhibited excellent reversibility after applying adsorption-desorption cycles. The excellent reversibility of the samples confirms that the CO_2 molecules were connected to the carbon surface by weak Van der Waals forces characteristic of the physical adsorption process [66].

The adsorption isotherms measured at 298 K, 308 K and 323 K were used to calculate the isosteric heats of CO_2 adsorption, corresponding to the heat released during the adsorption of CO_2 on the carbon surface. The adsorption isosteres are shown in Fig. S8. Table S1 lists and Fig. 9b shows the dependence of isosteric heats of CO_2 adsorption (ΔH_{st}) on surface coverage for the series of post-synthesized and activated 3DOmm carbon materials. At an adsorption of 0.5 mmol/g, the ΔH_{st} was within the range of 19.98–29.2 kJ/mol for the carbon samples, where the initial non-activated 3DOmm carbon revealed the lowest ΔH_{st} value and the 3DOmm-973K carbon showed the highest value of ΔH_{st}. With the increase in V_{CO2} there was a very small decrease in isosteric heat for the 3DOmm carbon (19.25 kJ/mol at 7 mmol/g). The activated 3DOmm carbon samples showed a more rapid decline in ΔH_{st} with increasing adsorption capacity at the beginning (up to ~2 mmol/g) followed by a slight decrease. At the adsorption capacity of 8 mmol/g, the isosteric heats were in the range of 18.9–22.3 kJ/mol.

Table 5
Results from pseudo-first order (PFO) and pseudo-second order (PSO) fittings of the kinetics data measured for a pressure step from 0 to 100 kPa at 298 K.

	PFO			PSO		
	k_1 (min^{-1})	R^2	RMSE	k_2 (min^{-1})	R^2	RMSE
3DOmm	0.2217	0.9932	0.0739	0.2473	0.9691	0.2200
3DOmm-973K	0.1616	0.9840	0.1071	0.1753	0.9706	0.2030
3DOmm-1073K	0.2187	0.9928	0.1174	0.1029	0.9837	0.2166
3DOmm-1173K	0.2260	0.9924	0.1298	0.1593	0.9673	0.3645

k_1 and k_2 are kinetic constants from PFO and PSO, respectively, R^2 is correlation coefficient, *RMSE* is root-mean-square deviation.

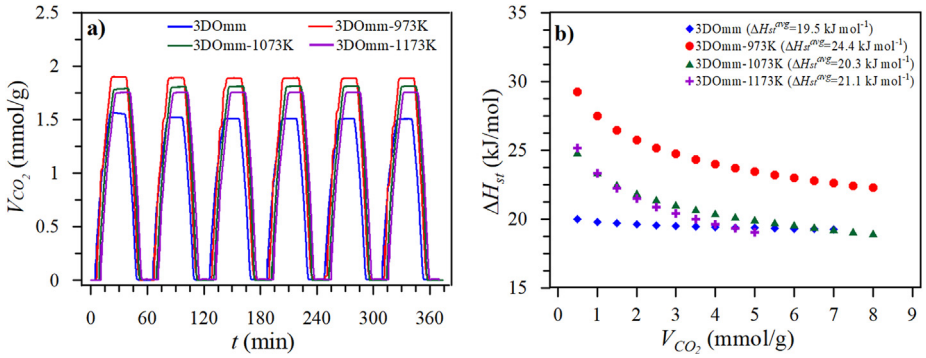

Fig. 9. a) time-dependent CO_2 cycles obtained on the 3DOmm carbon samples at 298 K and 100 kPa and b) Isosteric heats of CO_2 adsorption depending on surface coverage.

The isosteric heats determined for the 3DOmm carbons were less than 50 kJ/mol, indicating that the physical adsorption of CO_2 took place on the 3DOmm carbon surfaces [83,84]. The physical adsorption determined from the isosteric heats coincides nicely with the results obtained from the study of the regeneration ability of the carbon materials (Fig. 9a). The decrease in isosteric heats with adsorption suggested that the interaction of CO_2 molecules with the carbon surface was stronger than the interaction between CO_2 molecules; heterogeneous CO_2 adsorption also took place [85,86]. The values of isosteric heats and their trends were very similar for all 3DOmm carbons, indicating that similar adsorption sites were involved in CO_2 adsorption. The isosteric heats of CO_2 adsorption of the 3DOmm carbon materials were consistent with other porous carbon materials [68,87]. In contrast, carbon materials containing nitrogen functional groups showed stronger CO_2 – carbon surface interactions, resulting in higher ΔH_{st} values [33,43,70].

4. Conclusions

In this study, three-dimensionally ordered micromesoporous 3DOmm carbon was synthesized by the hard-templating method, followed by physical activation using CO_2 gas at different high temperatures to improve CO_2 capture ability. All 3DOmm carbon materials were characterised and then studied for CO_2 capture performance at atmospheric and higher pressures (up to 2 MPa) and at different temperatures. The 3DOmm carbons revealed an amorphous structure with a very low graphitization degree. Furthermore, the amount of disorder was more prominent in the carbon samples activated at temperatures above 973 K. It was also evident that activation did not have a destructive impact on the ordered structure. However, it was clearly seen that activation had a significant impact on pore volumes, which in turn had a significant impact on CO_2 adsorption performance over the whole range measured. The highest micropore and mesopore volumes and specific surface area were determined in the carbon sample activated at 973 K. A further increase in activating temperature led to a decrease in those parameters due to a broadening of the micropores and mesopores and shrinkage of the thin mesopore carbon walls. Exothermic CO_2 adsorption in the 3DOmm carbons varied with micropore volumes at atmospheric pressure and with mesopore volumes at higher pressures. The isosteric heats of adsorption indicated weak Van der Waals interactions between CO_2 molecules and the carbon surface, characteristic of physical adsorption. Physical adsorption was also confirmed from the kinetics results, where the pseudo first order model showed a perfect fit with the experimental data. It was also seen from the adsorption-desorption cycles that were performed, where perfect regenerative ability of the carbon materials was observed. The 3DOmm carbon samples showed high selectivity for CO_2 over N_2 at atmospheric pressure, depending on microporosity and fast adsorption kinetics.

This research reports the first study of the activated three-dimensionally ordered micromesoporous carbons synthesized by the hard-templating method investigated as adsorbents for CO_2 capture in a wide range of pressures and temperatures. It was found that the microporous structure of the 3DOmm carbon can be improved, leading to a better CO_2 capture performance in the whole pressure range. Comparison of the estimated CO_2 adsorption capacity of the 3DOmm carbons studied with other known carbon materials in the literature indicated that the physically activated 3DOmm carbon at 973 K has a big potential to be used as an adsorbent at different pressures, especially in the case of the pre-combustion capture. The above findings are essential in the field of material sciences, particularly in the design of advanced highly structured ordered microporous and mesoporous sustainable carbon adsorbents which might have a potential to be candidates for CO_2 capture, especially at high pressures due to a superior CO_2 capture performance and the reusability.

Credit author statement

Maryna Vorokhta: Writing – Original draft, Methodology, Investigation, Funding acquisition. **Jaroslava Nováková**: Investigation, Methodology. **Milan Dopita**: Investigation, Methodology. **Ivan Khalakhan**: Investigation, Methodology. **Vladimír Kopecký**: Investigation, Methodology. **Martina Švábová**: Investigation, Writing - Review & Editing.

Declaration of competing interest

The authors declare that they have no known competing financial interests or personal relationships that could have appeared to influence the work reported in this paper.

Data availability

No data was used for the research described in the article.

Acknowledgements

This work was supported by the research organization RVO: 67985891.

Appendix A. Supplementary data

Supplementary data to this article can be found online at https://doi.org/10.1016/j.mtsust.2023.100509.

References

[1] F. Chiang, O. Mazdiyasni, A. AghaKouchak, Evidence of anthropogenic impacts on global drought frequency, duration, and intensity, Nat. Commun. 12 (2021) 2754.

[2] Global carbon project, Supplemental Data of Global Carbon Budget 2021 (Version 1.0) [data set], 2021, https://www.icos-cp.eu/science-and-impact/global-carbon-budget/2020.

[3] Jet propulsion laboratory, National Aeronautics and Space Administration: NASA Global Climate Change and Global Warming: Vital Signs of the Planet, 2021. https://climate.nasa.gov/vital-signs/carbon-dioxide/.

[4] S.R. Shewchuk, A. Mukherjee, A.K. Dalai, Selective carbon-based adsorbents for carbon dioxide capture from mixed gas streams and catalytic hydrogenation of CO_2 into renewable energy source: a review, Chem. Eng. Sci. 243 (2021) 116735.

[5] X. Wang, C. Song, Carbon capture from flue gas and the atmosphere: a perspective, Front. Energy Res. 8 (2020) 560849.

[6] Earth system research laboratory, National Oceanic and Atmospheric Administration: Trends in Atmospheric Carbon Dioxide, 2021 (n.d.), https://www.esrl.noaa.gov/gmd/ccgg/trends/gl_full.html.

[7] F.O. Ochedi, Y. Liu, Y.G. Adewuyi, State-of-the-art review on capture of CO_2 using adsorbents prepared from waste materials, Process Saf. Environ. Protect. 139 (2020) 1–25.

[8] H. Sun, C. Wu, B. Shen, X. Zhang, Y. Zhang, J. Huang, Progress in the development and application of CaO-based adsorbents for CO_2 capture – a review, Mater. Today Sustain. 1–2 (2018) 1–27.

[9] Z. Dai, L. Deng, Membrane absorption using ionic liquid for pre-combustion CO_2 capture at elevated pressure and temperature, Int. J. Greenh. Gas Control 54 (2016) 59–69.

[10] K.C. Chen, J.Y. Lee, C.L. Chen, Hollow fiber-based rapid temperature swing adsorption process for carbon capture from coal-fired power plants, Sep. Purif. Technol. 247 (2020) 116958.

[11] H.M. Coromina, D.A. Walsh, R. Mokaya, Biomass-derived activated carbon with simultaneously enhanced CO_2 uptake for both pre and post combustion capture applications, J. Mater. Chem. A 4 (2015) 280–289.

[12] S.-M. Hong, E. Jang, A.D. Dysart, V.G. Pol, K.B. Lee, CO_2 capture in the sustainable wheat-derived activated microporous carbon compartments, Sci. Rep. 6 (2016) 34590.

[13] L. Luo, C. Yang, X. Yang, F. Liu, X. Wang, P. Chen, T. Zhao, Construction of ultramicroporous activated carbons derived from waste distiller's grains for efficient CO_2 adsorption, Sep. Purif. Technol. 302 (2022) 122134.

[14] K. Ramadass, C.I. Sathish, S. Mariaruban, G. Kothandam, S. Joseph, G. Singh, S. Kim, W. Cha, A. Karakoti, T. Belperio, J.B. Yi, A. Vinu, Carbon nanoflakes and nanotubes from halloysite nanoclays and their superior performance in CO_2 capture and energy storage, ACS Appl. Mater. Interfaces 12 (2020) 11922–11933.

[15] I.M. Maulana Kusdhany, M. Kusdhany, Z. Ma, A. Mufundirwa, H. Li, K. Sasaki, A. Hayashi, M.S. Lyth, Hydrogen and carbon dioxide uptake on scalable and inexpensive microporous carbon foams, Microporous Mesoporous Mater. 343 (2022) 112141.

[16] W. Wang, Z. Wang, L. Jiang, X. Shen, Y. Wang, R. Zhu, Z. Shen, X. Xu, Y. Liu, X. Li, J. Wang, Construction of hierarchically porous carbon from plastic waste for CO_2 capture and separation, Mater. Today Sustain. 21 (2023) 100280.

[17] L. Xie, J. Ding, X. Kong, J. Qin, J. Wang, Microwave-assisted synthesis of Mg-gallate for efficient CO_2 capture, Mater. Today Sustain. 22 (2023) 100356.

[18] P. Wang, G. Zhang, W. Chen, Q. Chen, H. Jiao, L. Liu, X. Wang, X. Deng, Molten salt template synthesis of hierarchical porous nitrogen-containing activated carbon derived from chitosan for CO_2 capture, ACS Omega 5 (2020) 23460–23467.

[19] M.E. Casco, M. Martínez-Escandell, J. Silvestre-Albero, F. Rodríguez-Reinoso, Effect of the porous structure in carbon materials for CO_2 capture at atmospheric and high-pressure, Carbon 67 (2014) 230–235.

[20] L.M. Esteves, T.J. Ferreira, A. Keba, J.M.S.S. Esperança, I.A.A.C. Esteves, Carbon materials derived from cyano-based IL@ZIF-8 composites for CO_2 sorption separation systems, Mater. Today Sustain. 22 (2023) 100353.

[21] I. Pełech, D. Sibera, P. Staciwa, U. Narkiewicz, R. Cormia, Pressureless and low-pressure synthesis of microporous carbon spheres applied to CO_2 adsorption, Molecules 25 (2021) 5328.

[22] A. Rehman, S.J. Park, From chitosan to urea-modified carbons: tailoring the ultra-microporosity for enhanced CO_2 adsorption, Carbon 159 (2020) 625–637.

[23] J. Serafin, K. Kiełbasa, B. Michalkiewicz, The new tailored nanoporous carbons from the common polypody (Polypodium vulgare): the role of textural properties for enhanced CO_2 adsorption, Chem. Eng. J. 429 (2022) 131751.

[24] M. Sevilla, A.S.M. Al-Jumialy, A.B. Fuertes, R. Mokaya, Optimization of the pore structure of biomass-based carbons in relation to their use for CO_2 capture under low- and high-pressure regimes, ACS Appl. Mater. Interfaces 10 (2018) 1623–1633.

[25] G. Chandrasekar, W.J. Son, W.S. Ahn, Synthesis of mesoporous materials SBA-15 and CMK-3 from fly ash and their application for CO_2 adsorption, J. Porous Mater. 16 (2009) 545–551.

[26] S. Yu, L. Wang, Q. Li, Y. Zhang, H. Zhou, Sustainable carbon materials from the pyrolysis of lignocellulosic biomass, Mater. Today Sustain. 19 (2022) 100209.

[27] D. Saha, M.J. Kienbaum, Role of oxygen, nitrogen and sulfur functionalities on the surface of nanoporous carbons in CO_2 adsorption: a critical review, Microporous Mesoporous Mater. 287 (2019) 29–55.

[28] C. Quan, H. Wang, X. Jia, N. Gao, Effect of carbonization temperature on CO_2 adsorption behavior of activated coal char, J. Energy Inst. 97 (2021) 92–99.

[29] Y.H. Abdelmoaty, T.D. Tessema, N. Norouzi, O.M. El-Kadri, J.B.M.G. Turner, H.M. El-Kaderi, Effective approach for increasing the heteroatom doping levels of porous carbons for superior CO_2 capture and separation performance, ACS Appl. Mater. Interfaces 9 (2017) 35802–35810.

[30] A. Rehman, G. Nazir, K.Y. Rhee, S.J. Park, Valorization of orange peel waste to tunable heteroatom-doped hydrochar-derived microporous carbons for selective CO_2 adsorption and separation, Sci. Total Environ. 849 (2022) 157805.

[31] E. Mawunya Kutorglo, J. Kovačovič, D. Trunov, F. Hassouna, A. Fučíková, D. Kopecký, I. Sedlářová, M. Šoóš, Preparation of carbon-based monolithic CO_2 adsorbents with hierarchical pore structure, Chem. Eng. J. 388 (2020) 124308.

[32] X. Ma, L. Li, R. Chen, C. Wang, H. Li, S. Wang, Heteroatom-doped nanoporous carbon derived from MOF-5 for CO_2 capture, Appl. Surf. Sci. 435 (2018) 494–502.

[33] E. Maruccia, A. Piovano, M.A.O. Lourenço, T. Priamushko, M. Cavallo, S. Bocchini, F. Bonino, F.C. Pirri, F. Kleitz, C. Gerbaldi, Revealing the competitive effect of N_2 and H_2O towards CO_2 adsorption in N-rich ordered mesoporous carbons, Mater. Today Sustain. 21 (2023) 100270.

[34] Y. Mochizuki, J. Bud, E. Byambajav, N. Tsubouchi, Influence of ammonia treatment on the CO_2 adsorption of activated carbon, J. Environ. Chem. Eng. 10 (2022) 107273.

[35] L. Tao, Q. Zhang, T. Li, S. Deng, Mild-temperature regenerable modified activated carbon fiber felt loaded with epoxide-modified aminating agents for efficient CO_2 capture from simulated indoor air, J. Environ. Chem. Eng. 10 (2022) 108620.

[36] Y. Xu, Z. Yang, G. Zhang, P. Zhao, Excellent CO_2 adsorption performance of nitrogen-doped waste biocarbon prepared with different activators, J. Clean. Prod. 264 (2020) 121645.

[37] C. Chen, Y. Yu, C. He, L. Wang, H. Huang, R. Albilali, J. Cheng, Z. Hao, Efficient capture of CO_2 over ordered micro-mesoporous hybrid carbon nanosphere, Appl. Surf. Sci. 439 (2018) 113–121.

[38] M.G. Plaza, C. Pevida, A. Arenillas, F. Rubiera, J.J. Pis, CO_2 capture by adsorption with nitrogen enriched carbons, Fuel 86 (2007) 2204–2212.

[39] A. Rehman, G. Nazir, K. Yop Rhee, S.J. Park, A rational design of cellulose-based heteroatom-doped porous carbons: promising contenders for CO_2 adsorption and separation, Chem. Eng. J. 420 (2021) 130421.

[40] Z. Zhang, N. Sun, W. Wei, Facile and controllable synthesis of ordered mesoporous carbons with tunable single-crystal morphology for CO_2 capture, Carbon 161 (2020) 629–638.

[41] S. Nithin Mithra, S.S. Ahankari, Nanocellulose-based membranes for CO_2 separation from biogas through the facilitated transport mechanism: a review, Mater. Today Sustain. 19 (2022) 100191.

[42] G. Nazir, A. Rehman, S.J. Park, Self-activated, urea modified microporous carbon cryogels for high-performance CO_2 capture and separation, Carbon 192 (2022) 14–29.

[43] G. Singh, K. Ramadass, J.M. Lee, I.S. Ismail, M. Singh, V. Bansal, J.H. Yang, A. Vinu, Convenient design of porous and heteroatom self-doped carbons for CO_2 capture, Microporous Mesoporous Mater. 287 (2019) 1–8.

[44] M. Vorokhta, M.I.M. Kusdhany, D. Vöröš, M. Nishihara, K. Sasaki, S.M. Lyth, Microporous carbon foams: the effect of nitrogen-doping on CO_2 capture and separation via pressure swing adsorption, Chem. Eng. J. 471 (2023) 144524.

[45] G. Nazir, A. Rehman, S.J. Park, Role of heteroatoms (nitrogen and sulfur)-dual doped corn-starch based porous carbons for selective CO_2 adsorption and separation, J. CO_2 Util. 51 (2021) 101641.

[46] G. Nazir, A. Rehman, S.J. Park, Valorization of shrimp shell biowaste for environmental remediation: efficient contender for CO_2 adsorption and separation, J. Environ. Manag. 299 (2021) 113661.

[47] M. Vorokhta, J. Morávková, M. Dopita, A. Zhigunov, M. Šlouf, R. Pilař, P. Sazama, Effect of micropores on CO_2 capture in ordered mesoporous CMK-3 carbon at atmospheric pressure, Adsorption 27 (2021) 1221–1236.

[48] H.M. Yoo, S.Y. Lee, S.J. Park, Ordered nanoporous carbon for increasing CO_2 capture, J. Solid State Chem. 197 (2013) 361–365.

[49] K. Cychosz, X. Guo, W. Fan, R. Cimino, Characterization of the pore structure of three-dimensionally ordered mesoporous carbons using high resolution gas sorption, Langmuir 28 (2012) 12647–12654.

[50] A. Vinu, P. Srinivasu, M. Takahashi, T. Mori, V.V. Balasubramanian, K. Ariga, Controlling the textural parameters of mesoporous carbon materials, Microporous Mesoporous Mater. 100 (2007) 20–26.

[51] M. Vorokhta, J. Morávková, D. Řimnáčová, R. Pilař, A. Zhigunov, M. Švábová, P. Sazama, CO_2 capture using three-dimensionally ordered micromesoporous carbon, J. CO_2 Util. 31 (2019) 124–134.

[52] International Organization for Standardization, Solid Mineral Fuels — Determination of Ash (ISO 1171:2010), Int. Stand., 2010. https://standards.iteh.ai/catalog/standards/sist/7e60fd7e-ee72-4a6e-a307-905fbcb91ced/iso-1171-2010.

[53] C. Nguyen, D.D. Do, The Dubinin-Radushkevich equation and the underlying microscopic adsorption description, Carbon 39 (2001) 1327–1336.
[54] E.D. Revellame, D.L. Fortela, W. Sharp, R. Hernandez, M.E. Zappi, Adsorption kinetic modeling using pseudo-first order and pseudo-second order rate laws: a review, Clean. Eng. Technol. 1 (2020) 100032.
[55] A. Mukherjee, B. Saha, C. Niu, A.K. Dalai, Preparation of activated carbon from spent coffee grounds and functionalization by deep eutectic solvent: effect of textural properties and surface chemistry on CO_2 capture performance, J. Environ. Chem. Eng. 10 (2022) 108815.
[56] B. Kaur, R.K. Gupta, H. Bhunia, Chemically activated nanoporous carbon adsorbents from waste plastic for CO_2 capture: breakthrough adsorption study, Microporous Mesoporous Mater. 282 (2019) 146–158.
[57] A.C. Ferrari, J. Robertson, Interpretation of Raman spectra of disordered and amorphous carbon, Phys. Rev. B 61 (2000) 14095–14107.
[58] S.M. Lyth, H. Shao, J. Liu, K. Sasaki, E. Akiba, Hydrogen adsorption on graphene foam synthesized by combustion of sodium ethoxide, Int. J. Hydrogen Energy 39 (2014) 376–380.
[59] K.S.W. Sing, D.H. Everett, R.A.W. Haul, L. Moscou, R.A. Pierotti, J. Rouquerol, T. Siemieniewska, Annexes: IUPAC recommendations: reporting physisorption data for gas/solid systems, Handb. Heterog. Catal. 3–5 (2008) 1503–1516.
[60] F.E.C. Othman, N. Yusof, S. Samitsu, N. Abdullah, M.F. Hamid, K. Nagai, M.N.Z. Abidin, M.A. Azali, A.F. Ismail, J. Jaafar, F. Aziz, W.N.W. Salleh, Activated carbon nanofibers incorporated metal oxides for CO_2 adsorption: effects of different type of metal oxides, J. CO_2 Util. 45 (2021) 101434.
[61] A. Ahmadpour, D.D. Do, The preparation of active carbons from coal by chemical and physical activation, Carbon 34 (1996) 471–479.
[62] A.N. Shafawi, A.R. Mohamed, P. Lahijani, M. Mohammadi, Recent advances in developing engineered biochar for CO_2 capture: an insight into the biochar modification approaches, J. Environ. Chem. Eng. 9 (2021) 106869.
[63] A. Rehman, S.J. Park, Environmental remediation by microporous carbon: an efficient contender for CO_2 and methylene blue adsorption, J. CO_2 Util. 34 (2019) 656–667.
[64] X. Ma, W. Xu, R. Su, L. Shao, Z. Zeng, L. Li, H. Wang, Insights into CO_2 capture in porous carbons from machine learning, experiments and molecular simulation, Sep. Purif. Technol. 306 (2023) 122521.
[65] E. Jang, S.W. Choi, S.M. Hong, S. Shin, K.B. Lee, Development of a cost-effective CO_2 adsorbent from petroleum coke via KOH activation, Appl. Surf. Sci. 429 (2018) 62–71.
[66] M.A. Al-Ghouti, D.A. Da'ana, Guidelines for the use and interpretation of adsorption isotherm models: a review, J. Hazard Mater. 393 (2020) 122383.
[67] A.F.M. EL-Mahdy, T.E. Liu, S.W. Kuo, Direct synthesis of nitrogen-doped mesoporous carbons from triazine-functionalized resol for CO_2 uptake and highly efficient removal of dyes, J. Hazard Mater. 391 (2020) 122163.
[68] M. Sevilla, A.B. Fuertes, CO_2 adsorption by activated templated carbons, J. Colloid Interface Sci. 366 (2012) 147–154.
[69] K. Chomiak, S. Gryglewicz, K. Kierzek, J. Machnikowski, Optimizing the properties of granular walnut-shell based KOH activated carbons for carbon dioxide adsorption, J. CO_2 Util. 21 (2017) 436–443.
[70] M.A. Khan, A.H. Javed, M. Qammar, M. Hafeez, M. Arshad, M.I. Zafar, A.M. Aldawsari, A. Shah, Z.U. Rehman, N. Iqbal, Nitrogen-rich mesoporous carbon for high temperature reversible CO_2 capture, J. CO_2 Util. 43 (2021) 101375.
[71] S. Ma, Y. Wang, Z. Liu, M. Huang, H. Yang, Z. liang Xu, Preparation of carbon nanofiber with multilevel gradient porous structure for supercapacitor and CO_2 adsorption, Chem. Eng. Sci. 205 (2019) 181–189.
[72] S. He, G. Chen, H. Xiao, G. Shi, C. Ruan, Y. Ma, H. Dai, B. Yuan, X. Chen, X. Yang, Facile preparation of N-doped activated carbon produced from rice husk for CO_2 capture, J. Colloid Interface Sci. 582 (2021) 90–101.
[73] A. Mukherjee, J.A. Okolie, A. Abdelrasoul, C. Niu, A.K. Dalai, Review of post-combustion carbon dioxide capture technologies using activated carbon, J. Environ. Sci. (China) 83 (2019) 46–63.
[74] J. Serafin, U. Narkiewicz, A.W. Morawski, R.J. Wróbel, B. Michalkiewicz, Highly microporous activated carbons from biomass for CO_2 capture and effective micropores at different conditions, J. CO_2 Util. 18 (2017) 73–79.
[75] S. Deng, B. Hu, T. Chen, B. Wang, J. Huang, Y. Wang, G. Yu, Activated carbons prepared from peanut shell and sunflower seed shell for high CO_2 adsorption, Adsorption 21 (2015) 125–133.
[76] F. Hussin, M.K. Aroua, R. Yusoff, Adsorption of CO_2 on palm shell based activated carbon modified by deep eutectic solvent: breakthrough adsorption study, J. Environ. Chem. Eng. 9 (2021) 105333.
[77] J. Bai, J. Huang, Q. Yu, M. Demir, F.H. Gecit, B.N. Altay, L. Wang, X. Hu, One-pot synthesis of self S-doped porous carbon for efficient CO_2 adsorption, Fuel Process. Technol. 244 (2023) 107700.
[78] C. Ma, J. Bai, M. Demir, X. Hu, S. Liu, L. Wang, Water chestnut shell-derived N/S-doped porous carbons and their applications in CO_2 adsorption and supercapacitor, Fuel 326 (2022) 125119.
[79] L. Pino, C. Italiano, A. Vita, C. Fabiano, V. Recupero, Sorbents with high efficiency for CO_2 capture based on amines-supported carbon for biogas upgrading, J. Environ. Sci. (China) 48 (2016) 138–150.
[80] Q. Yu, J. Bai, J. Huang, M. Demir, A.A. Farghaly, P. Aghamohammadi, X. Hu, L. Wang, One-pot synthesis of melamine formaldehyde resin-derived N-doped porous carbon for CO_2 capture application, Molecules 28 (2023) 1772.
[81] D.H. Everett, Thermodynamics of adsorption. III. Analysis and discussion of experimental data, Trans. Faraday Soc. 46 (1950) 957–969.
[82] X. Jian, P. Guan, W. Zhang, Carbon dioxide sorption and diffusion in coals: experimental investigation and modeling, Sci. China Earth Sci. 55 (2012) 633–643.
[83] K.S. Lakhi, W.S. Cha, J.H. Choy, M. Al-Ejji, A.M. Abdullah, A.M. Al-Enizi, A. Vinu, Synthesis of mesoporous carbons with controlled morphology and pore diameters from SBA-15 prepared through the microwave-assisted process and their CO_2 adsorption capacity, Microporous Mesoporous Mater. 233 (2016) 44–52.
[84] Q. Li, T. Lu, L. Wang, R. Pang, J. Shao, L. Liu, X. Hu, Biomass based N-doped porous carbons as efficient CO_2 adsorbents and high-performance supercapacitor electrodes, Sep. Purif. Technol. 275 (2021) 119204.
[85] C. Goel, H. Bhunia, P.K. Bajpai, Resorcinol–formaldehyde based nanostructured carbons for CO_2 adsorption: kinetics, isotherm and thermodynamic studies, RSC Adv. 5 (2015) 93563–93578.
[86] H. Yu, T. Li, X. Yang, C. Li, J. Mi, H. Meng, J. Jin, Hydrophobic carbon-based coating on metal tube with efficient and stable adsorption – desorption of CO_2 from wet flue gas, Sep. Purif. Technol. 307 (2023) 122798.
[87] C.M. Teague, J.A. Schott, C. Stieber, Z.E. Mann, P. Zhang, B.R. Williamson, S. Dai, S.M. Mahurin, Microporous and hollow carbon spheres derived from soft drinks: promising CO_2 separation materials, Microporous Mesoporous Mater. 286 (2019) 199–206.